

A record of plume-induced plate rotation triggering subduction initiation

Authors: Douwe J.J. van Hinsbergen^{1*}, Bernhard Steinberger^{2,3}, Carl Guilmette⁴, Marco Maffione^{1,5}, Derya Gürer^{1,6}, Kalijn Peters¹, Alexis Plunder^{1,7}, Peter J. McPhee¹, Carmen Gaina³, Eldert L. Advokaat^{1,5}, Reinoud L.M. Vissers¹, and Wim Spakman¹

Affiliations:

¹Department of Earth Sciences, Utrecht University, Princetonlaan 8A, 3584 CB Utrecht, Netherlands

²GFZ German Research Centre for Geosciences, Potsdam, Germany

³Centre of Earth Evolution and Dynamics (CEED), University of Oslo, Norway

⁴Département de Géologie et de Génie Géologique, Université Laval, Québec, QC G1K 7P4, Canada

⁵School of Geography, Earth and Environmental Sciences, University of Birmingham, B15 2TT, UK

⁶School of Earth and Environmental Sciences, University of Queensland, St Lucia, Queensland 4072, Australia

⁷BRGM, F-45060, Orléans, France

*Correspondence to: Douwe J.J. van Hinsbergen (d.j.j.vanhinsbergen@uu.nl)

22 **The formation of a global network of plate boundaries surrounding a mosaic of**
23 **lithospheric fragments was a key step in the emergence of Earth’s plate tectonics. So far,**
24 **propositions for plate boundary formation are regional in nature; how plate boundaries**
25 **are created over thousands of kilometers in geologically short periods remains elusive.**
26 **Here we show from geological observations that a >12,000 km-long plate boundary formed**
27 **between the Indian and African plates around 105 Ma. This boundary comprised**
28 **subduction segments from the eastern Mediterranean region to a newly established India-**
29 **Africa rotation pole in the west Indian ocean, where it transitioned into a ridge between**
30 **India and Madagascar. We identify coeval mantle plume rise below Madagascar-India as**
31 **the only viable trigger of this plate rotation. For this, we provide a proof of concept by**
32 **torque balance modeling, which reveals that the Indian and African cratonic keels were**
33 **important in determining plate rotation and subduction initiation in response to the**
34 **spreading plume head. Our results show that plumes may provide a non-plate-tectonic**
35 **mechanism for large plate rotation, initiating divergent and convergent plate boundaries**
36 **far away from the plume head. We suggest that this mechanism may be an underlying**
37 **cause of the emergence of modern plate tectonics.**

38 The early establishment of plate tectonics on Earth was likely a gradual process that
39 evolved as the cooling planet’s lithosphere broke into a mosaic of major fragments, separated by
40 a network of plate boundaries: spreading ridges, transform faults, and subduction zones¹. The
41 formation of spreading ridges and connecting transform faults is regarded as a passive process,
42 occasionally associated with rising mantle plumes². The formation of subduction zones is less
43 well understood. Explanations for subduction initiation often infer spontaneous gravitational
44 collapse of aging oceanic lithosphere², or relocations of subduction zones due to intraplate stress
45 changes in response to arrival of continents, oceanic plateaus, or volcanic arcs in trenches³.
46 Mantle plumes have also been suggested as drivers for regional subduction initiation, primarily
47 based on numerical modeling⁴⁻⁶. But while such processes may explain how plate tectonics
48 evolves on a regional scale, they do not provide insight into the geodynamic cause(s) for the
49 geologically sudden (<10 My) creation of often long (>1000 km) plate boundaries including new
50 subduction zones⁷. Demonstrating the causes of plate boundary formation involving subduction
51 initiation using the geological record is challenging and requires (i) establishing whether
52 subduction initiation was spontaneous or induced; (ii) if induced, constraining the timing and

53 direction of incipient plate convergence; (iii) reconstructing the entire plate boundary from triple
54 junction to triple junction, as well as the boundaries of neighboring plates, to identify collisions,
55 subduction terminations, or mantle plume arrival that may have caused stress changes driving
56 subduction initiation. In this paper, we provide such an analysis for an intra-oceanic subduction
57 zone that formed within the Neotethys Ocean around 105 Ma ago, to evaluate the driver of
58 subduction initiation and plate boundary formation.

59

60 **Induced subduction initiation across the Neotethys Ocean**

61 During induced subduction initiation, lower plate burial, dated through prograde mineral
62 growth in rocks of the incipient subduction plate contact, in so-called metamorphic soles⁸
63 predates upper plate extension that is inferred from spreading records in so-called supra-
64 subduction zone (SSZ) ophiolites^{8-10,11}. Such SSZ ophiolites have a chemical stratigraphy widely
65 interpreted as having formed at spreading ridges above a nascent subduction zone. Several SSZ
66 ophiolite belts exist in the Alpine-Himalayan mountain belt, which formed during the closure of
67 the Neotethys Ocean^{12,13} (Fig. 1A). One of these ophiolite belts formed in Cretaceous time and
68 runs from the eastern Mediterranean region, along northern Arabia, to Pakistan. Incipient lower
69 plate burial has been dated through Lu/Hf prograde garnet growth ages of ~104 Ma in
70 metamorphic soles in Oman as well as in the eastern Mediterranean region^{8,14}. Upper plate
71 extension and SSZ ophiolite spreading has been dated using magmatic zircon U/Pb ages and
72 synchronous metamorphic sole ⁴⁰Ar/³⁹Ar cooling ages and occurred at 96-95 Ma (Pakistan,
73 Oman)^{15,16} to 92-90 Ma (Iran, eastern Mediterranean region)¹⁷. The 8-14 Myr time delay
74 between initial lower plate burial and upper plate extension demonstrates that subduction
75 initiation was induced⁸.

76 An initial ~E-W convergence direction at this subduction zone was constrained through
77 paleomagnetic analysis and detailed kinematic reconstruction of post-subduction initiation
78 deformation of the eastern Mediterranean region, Oman, and Pakistan, and was accommodated at
79 ~N-S striking trench segments^{13,18-20}. This is surprising: for hundreds of Ma and throughout the
80 Tethyan realm, rifts and ridges accommodated the separation of continental fragments off
81 northern Gondwana in the south and their accretion to the southern Eurasian margin at
82 subduction zones in the north^{21,22}. The ~E-W convergence that triggered ~105 Ma subduction

83 initiation across the Neotethys ocean was thus near orthogonal to the long-standing plate
84 motions. To find the trigger inducing this subduction, we developed the first comprehensive
85 reconstruction of the entire ~12,000 km long plate boundary that formed at ~105 Ma and placed
86 this in context of reconstructions of collisions and mantle plumes of the Neotethyan realm (Fig.
87 1).

88

89 **Geological reconstruction of incipient plate boundary**

90 The SSZ ophiolites that formed at the juvenile Cretaceous intra-Neotethyan subduction
91 zone are now found as klippen on intensely deformed accretionary orogenic belts (Fig. 1A) that
92 formed when the continents of Greater Adria, Arabia, and India arrived in subduction zones. We
93 reconstructed these orogenic belts (Fig. 1) and restored these continents, and the Cretaceous
94 ophiolites that were thrust upon these, into their configuration at 105 Ma (Fig. 1C) (see
95 Methods).

96 The westernmost geological record of the Cretaceous intra-Neotethyan subduction zone
97 is found in eastern Greece and western Turkey, where it ended in a trench-trench-trench triple
98 junction with subduction zones along the southern Eurasian margin¹⁸. From there, east-dipping
99 (in the west) and west-dipping (in the east) subduction segments followed the saw-toothed shape
100 of the Greater Adriatic and Arabian continental margins (Fig. 1C) and initiated close to it: rocks
101 of these continental margins already underthrust the ophiolites within 5-15 My after SSZ
102 ophiolite spreading^{14,23,24}, and continent-derived zircons have been found in metamorphic sole
103 rocks²⁵. Subduction segments likely nucleated along ancient N-S and NE-SW trending fracture
104 zones and linked through highly oblique, north-dipping subduction zones that trended parallel to
105 and likely reactivated the pre-existing (hyper)extended passive margins (Fig. 1B, C)^{20,23}.
106 Subducted remnants of the Cretaceous intra-Neotethyan subduction are well-resolved in the
107 present-day mantle as slabs in the mid-mantle below the southeastern Mediterranean Sea, central
108 Arabia and the west Indian Ocean²⁶.

109 East of Arabia, we trace the intra-oceanic plate boundary to a NE-SW striking, NW-
110 dipping subduction zone between the Kabul Block and the west Indian passive margin. The 96
111 Ma Waziristan ophiolites of Pakistan formed above this subduction zone, perhaps by inverting an
112 Early Cretaceous spreading ridge between the Kabul Block and India¹³ and were thrust eastward

113 onto the Indian margin^{13,16} (Fig. 1B, C). The Cretaceous intra-Neotethyan plate boundary may
114 have been convergent to the Amirante Ridge in the west Indian Ocean¹³, from where it became
115 extensional instead and developed a rift, and later a spreading ridge, in the Mascarene Basin that
116 accommodated separation of India from Madagascar^{13,27,28} (Fig. 1B). The plate boundary ended
117 in a ridge-ridge-ridge triple junction in the south Indian Ocean^{13,28} (Fig. 1B).

118 The newly formed Cretaceous plate boundary essentially temporarily merged a large part
119 of Neotethyan oceanic lithosphere between Arabia and Eurasia to the Indian plate. This plate was
120 >12,000 km long from triple junction to triple junction, and reached from 45°S to 45°N, with
121 4500 km of rift/ridge in the southeast and 7500 km of subduction zone in the northwest and with
122 a transition between the convergent and divergent segments, representing the India-Africa Euler
123 pole¹³, in the west Indian Ocean, at a latitude between Pakistan and the Amirante Ridge (Fig.
124 1B). Marine geophysical constraints show a ~4° counterclockwise rotation of India relative to
125 Africa about the west Indian Ocean Euler pole during rifting preceding the ~83 Ma onset of
126 oceanic spreading in the Mascarene Basin²⁷⁻²⁹, associated with up to hundreds of km of ~E-W
127 convergence across the Neotethys (Fig. 1D).

128 The neighboring plates of the intra-Neotethyan subduction zone at 105 Ma were thus
129 Africa and India. The African plate was mostly surrounded by ridges and had a complex
130 subduction plate boundary in the Mediterranean region³⁰. The Indian plate was surrounded by
131 ridge-transform systems in the south and east and by subduction in the north, and may have
132 contained rifts and ridges between the Indian continent and Eurasia^{13,28}. The Neotethys
133 lithosphere between Arabia-Greater Adria and Eurasia continued unbroken to the north-dipping
134 subduction zone that had already existed along the southern Eurasian margin since the
135 Jurassic^{31,32}: the spreading ridges that existed during Neotethys Ocean opening in the Permian-
136 Triassic (north of Arabia)³³, and Triassic-Jurassic (eastern Mediterranean region)²³ had already
137 subducted below Eurasia before 105 Ma^{19,33} (Fig. 1B, C).

138

139 **Identifying potential drivers of subduction initiation**

140 Candidate processes to trigger the reconstructed plate boundary formation at 105 Ma are
141 terminations of existing subduction zones by arrival of buoyant lithosphere or the rise of mantle
142 plumes. Southern Eurasia contains relics of many microcontinents that accreted at or clogged

143 subduction zones since the Paleozoic, but none of these events started or ended around 105
144 Ma^{13,21-23,33-35}. Continental subduction and collision was ongoing in the central Mediterranean
145 region²³, but it is not evident how this or any other changes in subduction dynamics along the E-
146 W trending southern Eurasian margin would lead to E-W convergence in the Neotethys Ocean.
147 In the eastern Neotethys, a mid-Cretaceous collision of the intra-oceanic Woyla Arc with the
148 Sundaland continental margin led to a subduction polarity reversal initiating eastward subduction
149 below Sundaland³⁶, which is recorded in ophiolites on the Andaman Islands. There, metamorphic
150 sole rocks with ⁴⁰Ar/³⁹Ar hornblende cooling ages of 105-106 Ma, and likely coeval SSZ
151 ophiolite spreading ages³⁷ reveal that this subduction zone may have developed slab pull around
152 the same time as the Indian Ocean-western Neotethys plate boundary formed (Fig 1C). However,
153 eastward slab pull below Sundaland cannot drive E-W convergence in the Neotethys to the west,
154 and Andaman SSZ extension may well be an expression rather than the trigger of Indian plate
155 rotation. We find no viable plate tectonics-related driver of the ~105 Ma plate boundary
156 formation that we reconstructed here.

157 A key role, however, is possible for the only remaining geodynamic, non-plate-tectonic,
158 plate-motion driver in the region: a mantle plume. India-Madagascar continental breakup is
159 widely viewed^{13,27,37} as related to the ~94 Ma and younger formation of the Morondava Large
160 Igneous Province (LIP) on Madagascar³⁸ and southwest India³⁹. This LIP, however, started
161 forming ~10 Ma after initial plate boundary formation. To understand whether the plume may be
162 responsible for both LIP emplacement and plate boundary formation, we explore existing
163 numerical models of plume-plate interaction and conduct explorative torque-balance simulations
164 of plume-lithosphere interaction.

165

166 **Mantle plumes driving subduction initiation**

167 Numerical simulations of plume-lithosphere interaction have already identified that
168 plume head spreading below the lithosphere leads to horizontal asthenospheric flow that exerts a
169 ‘plume push’ force on the base of the lithosphere, particularly in the presence of a cratonic
170 keel^{5,40,41}. Plume push may accelerate plates by several cm/yr⁴¹ and has been proposed as a
171 potential driver of subduction initiation⁵.

172 In many cases, including in the case of the Morondava LIP, LIP eruption and
173 emplacement shortly preceded continental breakup, but pre-break up rifting preceded LIP
174 emplacement by 10-15 Myr²⁷. This early rifting typically is interpreted to indicate that the plume
175 migrated along the base of the lithosphere into a pre-existing rift that formed independently of
176 plume rise²⁷. However, in numerical simulations dynamic uplift⁴² and plume push⁴¹ already start
177 to accelerate plates 10-15 Myr before the plume head reaches the base of the lithosphere and
178 emplaces the LIP. Numerical simulations thus predict the observed delay between plume push,
179 as a driver for early rifting and subduction initiation, and LIP eruption and emplacement.

180 Here, we add to these plume-lithosphere coupling experiments by conducting proof-of-
181 concept torque-balance simulations particularly exploring why the observed India-Africa Euler
182 pole is so close to the plume head such that the associated plate rotation between Africa and
183 India caused E-W convergence in the Neotethys. We performed semi-analytical computations,
184 including both the Indian and African plates at ~105 Ma, and assess the influence of cratonic
185 keels on the position of the India-Africa Euler pole (Fig. 2, see Methods).

186 In our computations without cratonic keels, plume push under Madagascar/India caused
187 counterclockwise rotation of India versus Africa, but about an Euler pole situated far north of
188 Arabia, (Fig. 2A) without inducing significant E-W convergence within the Neotethys. However,
189 in experiments that include keels of the Indian and African cratonic lithosphere, which are
190 strongly coupled to the sub-asthenospheric mantle, the computed Euler pole location is shifted
191 southward towards the Indian continent, inducing E-W convergence along a larger part of the
192 plate boundary within the Neotethys Ocean (Fig. 2B).

193 Convergence of up to several hundreds of km, sufficient to induce self-sustaining
194 subduction²⁷, is obtained if plume material is fed into – and induced flow is confined to – a 200
195 km thick weak asthenospheric layer. The thinner this layer is, the further the plume head spreads,
196 and pushes the plate. The modern Indian cratonic root used in our computations has likely eroded
197 considerably during interaction with the ~70-65 Ma Deccan plume⁴³. India may have had a
198 thicker and/or laterally more extensive cratonic root at ~105 Ma than modeled here which would
199 further enhance coupling of the lithosphere and the sub-asthenospheric mantle. Furthermore, an
200 Euler pole close to India and a long convergent boundary to the north requires much weaker
201 coupling in the northern (oceanic) part of the India plate (Fig. 2). In this case, results remain

202 similar as long as the plume impinges near the southern part of the western boundary of
203 continental India.

204 An order of magnitude estimate of the maximum plume-induced stresses, assuming no
205 frictional resistance at other plate boundaries, is obtained from the rising force of $\sim 1.5 \cdot 10^{20}$ N of
206 a plume head with 1000 km diameter and density contrast 30 kg/m^3 . If half of this force acts on
207 the India plate and with a lever arm of 4000 km, this corresponds to a torque of $3 \cdot 10^{26}$ Nm. Once,
208 at the onset of rifting, ridge push is established as an additional force in the vicinity of the plume,
209 we estimate that this number may increase by up to a few tens of per cent. This torque can be
210 balanced at the convergent boundary (length ~ 5000 km, plate thickness ~ 100 km) involving
211 stresses of ~ 240 MPa, much larger than estimates of frictional resistance between subducting and
212 overriding plates that are only of the order of tens of MPa⁴⁴. For this estimate, we neglect any
213 frictional resistance at the base of the plate and at any other plate boundary – essentially
214 considering the plate as freely rotating above a pinning point. This is another endmember
215 scenario, as opposed to our above convergence estimate, where we had considered friction at the
216 plate base but neglected it at all plate boundaries. Therefore, the estimate of 240 MPa may be
217 considered as an upper bound but being compressive and oriented in the right direction it shows
218 the possibility of subduction initiation as has occurred in reality along the likely weakened
219 passive margin region of Arabia and Greater Adria. Moreover, the plume-induced compressive
220 stresses may have added to pre-existing compressive stresses, in particular due to ridge-push
221 around the African and Indian plates. Such additional compressive stresses may contribute to
222 shifting the Euler pole further south, closer to the position reconstructed in Fig. 1.

223 Subduction became self-sustained ~ 8 -12 Ma after its initiation, as marked by the 96-92
224 Ma age of SSZ spreading^{15,17}: inception of this spreading shows that subduction rates exceeded
225 convergence rates, and reconstructed SSZ spreading rates were an order of magnitude higher¹⁵
226 than Africa-Arabia or Indian absolute plate motions^{41,45} signaling slab roll-back, i.e. self-
227 sustained subduction^{20,46}. Numerical models suggest that self-sustained subduction may start
228 after ~ 50 -100 km of induced convergence⁷, corresponding to $\sim 1^\circ$ of India-Africa rotation
229 between ~ 105 and ~ 96 -92 Ma. Subsequent east and west-dipping subduction segments (Fig. 1)
230 may have contributed to and accelerated the India-Africa/Arabia rotation, driving the
231 propagation of the Euler pole farther to the south (compare Fig. 2A, C).

232

233 **Mantle plumes as an initiator of plate tectonics?**

234 Previously, numerical modeling has shown that mantle plumes may trigger circular
235 subduction initiation around a plume head⁴, where local plume-related convection may drive
236 subduction of thermally weakened lithosphere. This subduction would propagate through slab
237 roll-back and may have started the first subduction features on Earth⁴. 3D convective models do
238 produce a global network of plate boundaries^{47,48} but the role of plumes in initiating new
239 subduction zones within this network is unclear. Here, we have provided the first evidence that
240 plume rise formed a >12,000 km long plate boundary composed of both convergent and
241 divergent segments. Our documented example is Cretaceous in age but geological observations
242 showing a general temporal overlap between LIP emplacement and formation of SSZ ophiolite
243 belts over more than a billion years⁴⁹ suggest that plume rise is a key driving factor in the
244 formation of subduction plate boundaries. Because mantle plumes are thought to be also
245 common features on planets without plate tectonics, such as Mars and Venus⁵⁰, they may have
246 played a vital role in the emergence of modern style plate tectonics on Earth. That plumes may
247 have been key for the evolution of plate tectonics on Earth, as we suggest, but apparently
248 insufficient on Mars and Venus, provides a new outlook on understanding the different planetary
249 evolutions.

250

251 **References:**

- 252 1 Lenardic, A. The diversity of tectonic modes and thoughts about transitions between them. *Philosophical*
253 *Transactions of the Royal Society A: Mathematical, Physical and Engineering Sciences* **376**, 20170416
254 (2018).
- 255 2 Stern, R. J. Subduction initiation: spontaneous and induced. *Earth and Planetary Science Letters* **226**, 275-
256 292, doi:10.1016/s0012-821x(04)00498-4 (2004).
- 257 3 Hall, C. E., Gurnis, M., Sdrolias, M., Lavier, L. L. & Müller, R. D. Catastrophic initiation of subduction
258 following forced convergence across fracture zones. *Earth and Planetary Science Letters* **212**, 15-30,
259 doi:10.1016/s0012-821x(03)00242-5 (2003).
- 260 4 Gerya, T. V., Stern, R. J., Baes, M., Sobolev, S. V. & Whattam, S. A. Plate tectonics on the Earth triggered
261 by plume-induced subduction initiation. *Nature* **527**, 221-225, doi:10.1038/nature15752 (2015).
- 262 5 Pusok, A. E. & Stegman, D. R. The convergence history of India-Eurasia records multiple subduction
263 dynamics processes. *Science Advances* **6**, eaaz8681 (2020).
- 264 6 Baes, M., Sobolev, S., Gerya, T. & Brune, S. Plume-Induced Subduction Initiation: Single-Slab or Multi-
265 Slab Subduction? *Geochemistry, Geophysics, Geosystems* **21**, e2019GC008663 (2020).
- 266 7 Gurnis, M., Hall, C. & Lavier, L. Evolving force balance during incipient subduction. *Geochemistry,*
267 *Geophysics, Geosystems* **5**, doi:10.1029/2003gc000681 (2004).
- 268 8 Guilmette, C. *et al.* Forced subduction initiation recorded in the sole and crust of the Semail Ophiolite of
269 Oman. *Nature Geoscience* **11**, 688-695 (2018).

270 9 Stern, R. J. & Gerya, T. Subduction initiation in nature and models: A review. *Tectonophysics*,
271 doi:10.1016/j.tecto.2017.10.014 (2017).

272 10 Agard, P. *et al.* Plate interface rheological switches during subduction infancy: Control on slab penetration
273 and metamorphic sole formation. *Earth and Planetary Science Letters* **451**, 208-220 (2016).

274 11 van Hinsbergen, D. J. J. *et al.* Dynamics of intraoceanic subduction initiation: 2. Suprasubduction zone
275 ophiolite formation and metamorphic sole exhumation in context of absolute plate motions. *Geochemistry,*
276 *Geophysics, Geosystems* **16**, 1771-1785, doi:10.1002/2015gc005745 (2015).

277 12 Dilek, Y. & Furnes, H. Ophiolite genesis and global tectonics: Geochemical and tectonic fingerprinting of
278 ancient oceanic lithosphere. *Geological Society of America Bulletin* **123**, 387-411, doi:10.1130/b30446.1
279 (2011).

280 13 Gaina, C., van Hinsbergen, D. J. J. & Spakman, W. Tectonic interactions between India and Arabia since
281 the Jurassic reconstructed from marine geophysics, ophiolite geology, and seismic tomography. *Tectonics*
282 **34**, 875-906, doi:10.1002/2014tc003780 (2015).

283 14 Pourteau, A. *et al.* Thermal evolution of an ancient subduction interface revealed by Lu–Hf garnet
284 geochronology, Halilbağ Complex (Anatolia). *Geoscience Frontiers* **10**, 127-148,
285 doi:10.1016/j.gsf.2018.03.004 (2019).

286 15 Rioux, M. *et al.* Synchronous formation of the metamorphic sole and igneous crust of the Semail ophiolite:
287 New constraints on the tectonic evolution during ophiolite formation from high-precision U–Pb zircon
288 geochronology. *Earth and Planetary Science Letters* **451**, 185-195 (2016).

289 16 Robinson, J., Beck, R., Gnos, E. & Vincent, R. K. New structural and stratigraphic insights for
290 northwestern Pakistan from field and Landsat Thematic Mapper data. *Geological Society of America*
291 *Bulletin* **112**, 364-374, doi:10.1130/0016-7606(2000)112<364:Nsasif>2.0.Co;2 (2000).

292 17 Parlak, O. The tauride ophiolites of Anatolia (Turkey): A review. *Journal of Earth Science* **27**, 901-934,
293 doi:10.1007/s12583-016-0679-3 (2016).

294 18 van Hinsbergen, D. J. J. *et al.* Tectonic evolution and paleogeography of the Kırşehir Block and the Central
295 Anatolian Ophiolites, Turkey. *Tectonics* **35**, 983-1014, doi:10.1002/ (2016).

296 19 Maffione, M., van Hinsbergen, D. J. J., de Gelder, G. I. N. O., van der Goes, F. C. & Morris, A. Kinematics
297 of Late Cretaceous subduction initiation in the Neo-Tethys Ocean reconstructed from ophiolites of Turkey,
298 Cyprus, and Syria. *Journal of Geophysical Research: Solid Earth* **122**, 3953-3976,
299 doi:10.1002/2016jb013821 (2017).

300 20 van Hinsbergen, D. J., Maffione, M., Koornneef, L. M. & Guilmette, C. Kinematic and paleomagnetic
301 restoration of the Semail ophiolite (Oman) reveals subduction initiation along an ancient Neotethyan
302 fracture zone. *Earth and Planetary Science Letters* **518**, 183-196 (2019).

303 21 Torsvik, T. H. & Cocks, L. R. M. *Earth history and palaeogeography*. 317 (Cambridge University Press,
304 2017).

305 22 Wan, B. *et al.* Cyclical one-way continental rupture-drift in the Tethyan evolution: Subduction-driven plate
306 tectonics. *Science China Earth Sciences*, 1-12 (2019).

307 23 van Hinsbergen, D. J. J. *et al.* Orogenic architecture of the Mediterranean region and kinematic
308 reconstruction of its tectonic evolution since the Triassic. *Gondwana Research* **81**, 79-229 (2020).

309 24 Warren, C. J., Parrish, R. R., Waters, D. J. & Searle, M. P. Dating the geologic history of Oman's Semail
310 ophiolite: insights from U-Pb geochronology. *Contributions to Mineralogy and Petrology* **150**, 403-422,
311 doi:10.1007/s00410-005-0028-5 (2005).

312 25 Güngör, T. *et al.* Kinematics and U-Pb zircon ages of the sole metamorphics of the Marmaris Ophiolite,
313 Lycian Nappes, Southwest Turkey. *International Geology Review* **61**, 1124-1142 (2019).

314 26 van der Meer, D. G., van Hinsbergen, D. J. J. & Spakman, W. Atlas of the underworld: Slab remnants in
315 the mantle, their sinking history, and a new outlook on lower mantle viscosity. *Tectonophysics* **723**, 309-
316 448, doi:10.1016/j.tecto.2017.10.004 (2018).

317 27 Buitter, S. J. & Torsvik, T. H. A review of Wilson Cycle plate margins: A role for mantle plumes in
318 continental break-up along sutures? *Gondwana Research* **26**, 627-653 (2014).

319 28 Gibbons, A. D., Whittaker, J. M. & Müller, R. D. The breakup of East Gondwana: Assimilating constraints
320 from Cretaceous ocean basins around India into a best-fit tectonic model. *Journal of Geophysical*
321 *Research: Solid Earth* **118**, 808-822, doi:10.1002/jgrb.50079 (2013).

322 29 Gaina, C., Müller, R. D., Brown, B., Ishihara, T. & Ivanov, S. Breakup and early seafloor spreading
323 between India and Antarctica. *Geophysical Journal International* **170**, 151-169, doi:10.1111/j.1365-
324 246X.2007.03450.x (2007).

325 30 Gaina, C. *et al.* The African Plate: A history of oceanic crust accretion and subduction since the Jurassic.
326 *Tectonophysics* **604**, 4-25, doi:10.1016/j.tecto.2013.05.037 (2013).

327 31 Agard, P., Jolivet, L., Vrielynck, B., Burov, E. & Monié, P. Plate acceleration: The obduction trigger?
328 *Earth and Planetary Science Letters* **258**, 428-441, doi:10.1016/j.epsl.2007.04.002 (2007).

329 32 Jolivet, L. *et al.* Neo-Tethys geodynamics and mantle convection: from extension to compression in Africa
330 and a conceptual model for obduction. *Canadian journal of earth sciences* **53**, 1190-1204 (2015).

331 33 Stampfli, G. M. & Borel, G. A plate tectonic model for the Paleozoic and Mesozoic constrained by
332 dynamic plate boundaries and restored synthetic oceanic isochrons. *Earth and Planetary Science Letters*
333 **196**, 17-33 (2002).

334 34 van Hinsbergen, D. J. J. *et al.* Reconstructing Greater India: Paleogeographic, kinematic, and geodynamic
335 perspectives. *Tectonophysics* **760**, 69-94, doi:10.1016/j.tecto.2018.04.006 (2019).

336 35 Kapp, P. & DeCelles, P. G. Mesozoic–Cenozoic geological evolution of the Himalayan-Tibetan orogen and
337 working tectonic hypotheses. *American Journal of Science* **319**, 159-254 (2019).

338 36 Advokaat, E. L. *et al.* Early Cretaceous origin of the Woyla Arc (Sumatra, Indonesia) on the Australian
339 plate. *Earth and Planetary Science Letters* **498**, 348-361 (2018).

340 37 Plunder, A. *et al.* History of subduction polarity reversal during arc-continent collision: constraints from the
341 Andaman Ophiolite and its metamorphic sole. *Tectonics*, e2019TC005762 (2020).

342 38 Torsvik, T. *et al.* Late Cretaceous magmatism in Madagascar: palaeomagnetic evidence for a stationary
343 Marion hotspot. *Earth and Planetary Science Letters* **164**, 221-232 (1998).

344 39 Mohan, M. R. *et al.* The Ezhimala igneous complex, southern India: Possible imprint of late Cretaceous
345 magmatism within rift setting associated with India–Madagascar separation. *Journal of Asian Earth*
346 *Sciences* **121**, 56-71 (2016).

347 40 Cande, S. C. & Stegman, D. R. Indian and African plate motions driven by the push force of the Reunion
348 plume head. *Nature* **475**, 47-52, doi:10.1038/nature10174 (2011).

349 41 van Hinsbergen, D. J. J., Steinberger, B., Doubrovine, P. V. & Gassmöller, R. Acceleration and
350 deceleration of India-Asia convergence since the Cretaceous: Roles of mantle plumes and continental
351 collision. *Journal of Geophysical Research* **116**, doi:10.1029/2010jb008051 (2011).

352 42 Wang, Y. & Li, M. The interaction between mantle plumes and lithosphere and its surface expressions: 3-D
353 numerical modelling. *Geophysical Journal International*, doi:10.1093/gji/ggab014 (2021).

354 43 Kumar, P. *et al.* The rapid drift of the Indian tectonic plate. *Nature* **449**, 894-897, doi:10.1038/nature06214
355 (2007).

356 44 Lamb, S. & Davis, P. Cenozoic climate change as a possible cause for the rise of the Andes. *Nature* **425**,
357 792-797 (2003).

358 45 van der Meer, D. G., Spakman, W., van Hinsbergen, D. J. J., Amaru, M. L. & Torsvik, T. H. Towards
359 absolute plate motions constrained by lower-mantle slab remnants. *Nature Geoscience* **3**, 36-40,
360 doi:10.1038/ngeo708 (2010).

361 46 Tavani, S., Corradetti, A., Sabbatino, M., Seers, T. & Mazzoli, S. Geological record of the transition from
362 induced to self-sustained subduction in the Oman Mountains. *Journal of Geodynamics* **133**, 101674 (2020).

363 47 Tackley, P. J. Mantle convection and plate tectonics: Toward an integrated physical and chemical theory.
364 *Science* **288**, 2002-2007 (2000).

365 48 Coltice, N., Husson, L., Faccenna, C. & Arnould, M. What drives tectonic plates? *Science Advances* **5**,
366 eaax4295 (2019).

367 49 Dilek, Y. Ophiolite pulses, mantle plumes and orogeny. *Geological Society, London, Special Publications*
368 **218**, 9-19 (2003).

369 50 Ernst, R., Grosfils, E. & Mege, D. Giant dike swarms: Earth, venus, and mars. *Annual Review of Earth and*
370 *Planetary Sciences* **29**, 489-534 (2001).

371 51 Müller, R. D. *et al.* GPlates: building a virtual Earth through deep time. *Geochemistry, Geophysics,*
372 *Geosystems* **19**, 2243-2261 (2018).

373 52 Clube, T. M. M., Creer, K. M. & Robertson, A. H. F. Palaeorotation of the Troodos microplate, Cyprus.
374 *Nature* **317**, 522, doi:10.1038/317522a0 (1985).

375 53 Morris, A., Meyer, M., Anderson, M. W. & MacLeod, C. J. Clockwise rotation of the entire Oman
376 ophiolite occurred in a suprasubduction zone setting. *Geology* **44**, 1055-1058 (2016).

377 54 McQuarrie, N. & van Hinsbergen, D. J. J. Retrodeforming the Arabia-Eurasia collision zone: Age of
378 collision versus magnitude of continental subduction. *Geology* **41**, 315-318, doi:10.1130/g33591.1 (2013).

379 55 Monsef, I. *et al.* Evidence for an early-MORB to fore-arc evolution within the Zagros suture zone:
380 Constraints from zircon U-Pb geochronology and geochemistry of the Neyriz ophiolite (South Iran).
381 *Gondwana Research* **62**, 287-305 (2018).

382 56 Galoyan, G. *et al.* Geology, geochemistry and ⁴⁰Ar/³⁹Ar dating of Sevan ophiolites (Lesser Caucasus,
383 Armenia): evidence for Jurassic Back-arc opening and hot spot event between the South Armenian Block
384 and Eurasia. *Journal of Asian Earth Sciences* **34**, 135-153 (2009).

385 57 Çelik, Ö. F. *et al.* Jurassic metabasic rocks in the Kızılırmak accretionary complex (Kargı region, Central
386 Pontides, Northern Turkey). *Tectonophysics* **672-673**, 34-49, doi:10.1016/j.tecto.2016.01.043 (2016).

387 58 Topuz, G. *et al.* Jurassic ophiolite formation and emplacement as backstop to a subduction-accretion
388 complex in northeast Turkey, the Refahiye ophiolite, and relation to the Balkan ophiolites. *American*
389 *Journal of Science* **313**, 1054-1087, doi:10.2475/10.2013.04 (2014).

390 59 Ao, S. *et al.* U–Pb zircon ages, field geology and geochemistry of the Kermanshah ophiolite (Iran): From
391 continental rifting at 79Ma to oceanic core complex at ca. 36Ma in the southern Neo-Tethys. *Gondwana*
392 *Research* **31**, 305-318, doi:10.1016/j.gr.2015.01.014 (2016).

393 60 Peters, T. & Mergalli, I. Extremely thin oceanic crust in the Proto-Indian Ocean: Evidence from the
394 Masirah Ophiolite, Sultanate of Oman. *Journal of Geophysical Research: Solid Earth* **103**, 677-689,
395 doi:10.1029/97jb02674 (1998).

396 61 Gnos, E. *et al.* Bela oceanic lithosphere assemblage and its relation to the Reunion hotspot. *Terra Nova* **10**,
397 90-95 (1998).

398 62 Tapponnier, P., Mattauer, M., Proust, F. & Cassaigneau, C. Mesozoic ophiolites, sutures, and large-scale
399 tectonic movements in Afghanistan. *Earth and Planetary Science Letters* **52**, 355-371 (1981).

400 63 van Hinsbergen, D. J. J. *et al.* Greater India Basin hypothesis and a two-stage Cenozoic collision between
401 India and Asia. *Proc Natl Acad Sci U S A* **109**, 7659-7664, doi:10.1073/pnas.1117262109 (2012).

402 64 Yuan, J. *et al.* Rapid drift of the Tethyan Himalaya terrane before two-stage India-Asia collision. *National*
403 *Science Review* (2020).

404 65 Hébert, R. *et al.* The Indus–Yarlung Zangbo ophiolites from Nanga Parbat to Namche Barwa syntaxes,
405 southern Tibet: First synthesis of petrology, geochemistry, and geochronology with incidences on
406 geodynamic reconstructions of Neo-Tethys. *Gondwana Research* **22**, 377-397,
407 doi:10.1016/j.gr.2011.10.013 (2012).

408 66 Zahirovic, S. *et al.* Tectonic evolution and deep mantle structure of the eastern Tethys since the latest
409 Jurassic. *Earth-Science Reviews* **162**, 293-337 (2016).

410 67 Huang, W. *et al.* Lower Cretaceous Xigaze ophiolites formed in the Gangdese forearc: Evidence from
411 paleomagnetism, sediment provenance, and stratigraphy. *Earth and Planetary Science Letters* **415**, 142-
412 153, doi:10.1016/j.epsl.2015.01.032 (2015).

413 68 Westerweel, J. *et al.* Burma Terrane part of the Trans-Tethyan arc during collision with India according to
414 palaeomagnetic data. *Nature Geoscience* **12**, 863-868 (2019).

415 69 Jagoutz, O., Royden, L., Holt, A. F. & Becker, T. W. Anomalously fast convergence of India and Eurasia
416 caused by double subduction. *Nature Geoscience* **8**, 475-478, doi:10.1038/ngeo2418 (2015).

417 70 Höink, T. & Lenardic, A. Long wavelength convection, Poiseuille–Couette flow in the low-viscosity
418 asthenosphere and the strength of plate margins. *Geophysical Journal International* **180**, 23-33 (2010).

419 71 Höink, T., Jellinek, A. M. & Lenardic, A. Viscous coupling at the lithosphere-asthenosphere boundary.
420 *Geochemistry, Geophysics, Geosystems* **12** (2011).

421 72 Campbell, I. H. Testing the plume theory. *Chemical Geology* **241**, 153-176 (2007).

422 73 Doubrovine, P. V., Steinberger, B. & Torsvik, T. H. A failure to reject: Testing the correlation between
423 large igneous provinces and deep mantle structures with EDF statistics. *Geochemistry, Geophysics,*
424 *Geosystems* **17**, 1130-1163 (2016).

425 74 Steinberger, B. Topography caused by mantle density variations: observation-based estimates and models
426 derived from tomography and lithosphere thickness. *Geophysical Journal International* **205**, 604-621
427 (2016).

428 75 Steinberger, B. & Becker, T. W. A comparison of lithospheric thickness models. *Tectonophysics* **746**, 325-
429 338 (2018).

432 **Corresponding author:** Douwe van Hinsbergen (d.j.j.vanhinsbergen@uu.nl)

433

434 **Acknowledgments:** DJJvH acknowledges funding through European Research Council Starting
435 Grant 306810 (SINK) (also funding MM, DG, AP, and ELA) Netherlands Organization
436 for Scientific Research (NWO) Vidi grant 864.11.004 (also funding KP and PJmcP) and
437 Netherlands Organization for Scientific Research (NWO) Vici grant 865.17.001. BS and
438 CGa received funding from the Research Council of Norway through its Centres of
439 Excellence funding scheme, project number 223272. BS acknowledges the innovation
440 pool of the Helmholtz Association through the “Advanced Earth System Modelling
441 Capacity (ESM)” activity. CG was funded through Discovery Grant (RGPIN-2014-
442 05681) from the National Science and Engineering Research Council of Canada. We
443 thank Inge Loes ten Kate and Debaditya Bandyopadhyay for discussion, and Fabio
444 Capitanio and Dietmar Müller for their comments.

445

446 **Author contributions:** DJJvH, BS, WS designed research. DJJvH, CGu, MM, DG, KP, AP,
447 PJmcP, CGa, ELA and RLMV developed the kinematic reconstruction; BS performed
448 modelling; DJJvH, BS, CGu, WS wrote the paper, all authors made corrections and edits.

449

450 **Competing interests:** All authors declare no competing interests.

451

452 **Fig. 1. Plate kinematic reconstructions of the Neotethys Ocean and surrounding continents.**

453 a) the present-day; b) 70 Ma; c) 105 Ma, corresponding to the timing of intra-Neotethyan
454 subduction initiation and d) 110 Ma, just before intra-Neotethyan subduction initiation. See
455 Methods for the plate reconstruction approach and sources of detailed restorations.

456 Reconstructions show in a mantle reference frame⁴⁵. AR = Amirante Ridge; Emed = Eastern
457 Mediterranean Region; Ir = Iran; LIP = Large Igneous Province; Mad = Madagascar; Mas =
458 Mascarene Basin; Pak = Pakistan, Tur = Turkey; Waz = Waziristan Ophiolite.

459

460 **Fig. 2. Torque balance modeling results of plumes affecting plates similar to India and**
461 **Africa with, and without cratonic keels.** The computed total displacement, induced by the
462 Morondava plume (pink circle) for the restored ~105 Ma plate configuration (Fig. 1c) for plates
463 without (a, b) and with (c, d) African and Indian cratonic keels, in an Africa-fixed (a, c), or
464 mantle reference frame⁴⁵ (b, d) (see Methods). Ten degree grid spacing; locations of plates,
465 lithosphere thickness and the plume are reconstructed in a slab-fitted mantle reference frame⁴⁵.

466

467 **Methods: Kinematic reconstruction** – The kinematic restoration of Neotethyan intra-
468 oceanic subduction was made in GPlates plate reconstruction software (www.gplates.org)⁵¹.
469 First, we systematically restored stable plates using marine geophysical data from the Atlantic
470 and Indian Ocean, and then restored continental margin deformation that occurred following the
471 arrival of continental lithosphere below the oceanic lithosphere preserved as ophiolites. These
472 restorations are based on a systematic reconstruction protocol, based on magnetic anomalies and
473 fracture zones of present-day sea floor and geophysical constraints on pre-drift extension in
474 adjacent passive continental margins²³, followed by kinematic restoration of post-obduction
475 orogenic deformation using structural geological constraints on continental extension, strike-slip
476 deformation, and shortening, and paleomagnetic constraints on vertical axis rotations. We then
477 restored pre-emplacement vertical axis microplate rotations^{52,53}, as well as paleo-orientations of
478 the SSZ spreading ridges at which the ophiolitic crust formed¹⁸⁻²⁰. The reconstruction shown in
479 Fig. 1B compiles kinematic restorations for the eastern Mediterranean region²³, Iran⁵⁴, Oman²⁰,
480 Pakistan¹³, and the Himalaya³⁴. Ophiolites interpreted to be part of the Cretaceous subduction
481 system include the 96-90 Ma, Cretaceous ophiolites exposed in SE Greece, Anatolia, Cyprus,
482 Syria, and Iraq, the Neyriz ophiolite of Iran, the Semail ophiolite in Oman, and the Waziristan-
483 Khost ophiolite in Pakistan and Afghanistan^{15-17,55}. The Jurassic ophiolite belts of northern
484 Turkey and Armenia⁵⁶⁻⁵⁸ and the late Cretaceous (<80 Ma) Kermanshah ophiolite of Iran⁵⁹ are
485 not included and are instead interpreted to have formed along the southern Eurasian margin²³.
486 The Masirah Ophiolite of East Oman⁶⁰ and the uppermost Cretaceous Bela, Muslim Bagh, and
487 Kabul-Altimur ophiolites of Pakistan and Afghanistan^{61,62} are interpreted to reflect oblique latest
488 Cretaceous to Paleogene India-Arabia convergence¹³ and are also unrelated to the event studied

489 here. Restoration of intra-oceanic subduction prior to the arrival of the continental margins used
490 paleomagnetic data from the ophiolites of Oman, Syria, Cyprus, and Turkey that constrain
491 vertical axis rotations, as well as the orientation of sheeted dyke following cooling after
492 intrusion^{18-20,52,53} as proxy for original ridge and intra-oceanic trench orientations. These
493 paleomagnetic data systematically revealed N-S to NW-SE primary sheeted dyke orientations¹⁸⁻
494 ^{20,52,53}. Because the ages of the SSZ ophiolites in the Neotethyan belt do not laterally progress,
495 spreading must have occurred near-orthogonal to the associated trench, which must thus also
496 have been striking N-S to NE-SW, as shown in the reconstruction of Fig. 1.

497 How far the Indian plate continued northwards around 105 Ma is subject to ongoing
498 debate. On the one hand, the northern Indian continental margin has been proposed to have rifted
499 off India sometime in the Cretaceous^{34,63}, but recent paleomagnetic data suggest that this process
500 occurred in the late Cretaceous, well after 100 Ma⁶⁴. Others inferred that the north Indian
501 continent had a passive margin contiguous with oceanic Neotethyan lithosphere since the middle
502 Jurassic or before and continued to a subduction zone below the SSZ ophiolites found in the
503 Himalayan suture zone and the Kohistan arc^{35,65,66}. Sedimentary and paleomagnetic data
504 demonstrate that these ophiolites formed adjacent to the Eurasian margin in the Early
505 Cretaceous⁶⁷, although they may have migrated southward during slab roll-back in the Late
506 Cretaceous³⁵. Recent paleomagnetic data have shown that a subduction zone may have existed
507 within the Neotethys to the west of the Andaman Islands, above which the West Burma Block
508 would have been located (Figure 1)⁶⁸. Our reconstruction of the eastern Neotethys may thus be
509 oversimplified. However, the geological record of the West Burma Block shows that this
510 subduction zone already existed as early as 130 Ma, and E-W trending until well into the
511 Cenozoic⁶⁸, and we see no reason to infer that changes in the eastern Neotethys contributed to
512 the plate boundary formation discussed here. Some have speculated that the West Burma
513 subduction zone would have been connected to a long-lived, equatorial subduction zone within
514 the Neotethys all along the Indian segment that would already have existed in the Early
515 Cretaceous⁶⁹: this scenario remains unconstrained by paleomagnetic data, and is inconsistent
516 with sediment provenance data from the Himalaya and overlying ophiolites³⁵. In summary, the
517 Indian plate around 105 Ma continued far into the Neotethyan realm, and the India-Africa
518 rotation is a likely driver of E-W convergence sparking subduction initiation close to the
519 northern Gondwana margin purported in Figure 1.

520 *Torque balance modeling* – Forces considered here include (i) the push due to plume-
521 induced flow in the asthenosphere and (ii) the drag due to shear flow between the moving plate
522 and a deeper mantle at rest (Fig. S1). In the first case, we disregard any lateral variations. Plume-
523 induced flow is treated as Poiseuille flow, i.e. with parabolic flow profile, in an asthenospheric
524 channel of thickness h_c , radially away from the plume stem. Since at greater distance plume-
525 induced flow will eventually not remain confined to the asthenosphere, we only consider it to a
526 distance 2400 km, in accord with numerical results⁴¹, and consistent with the finding that there is
527 a transition from dominantly pressure-driven Poiseuille flow at shorter wavelengths to
528 dominantly shear-driven Couette flow at length scales approximately exceeding mantle
529 depth^{70,71}. With v_0 the velocity in the center of the channel at a distance d from the plume stem
530 the total volume flux rate is $2/3 \times v_0 \times 2\pi d \times h_c$ (here neglecting the curvature of the Earth
531 surface for simplicity). Its time integral is equal to the volume of the plume head with radius
532 estimated⁷² to be about $r_p = 500$ km, with considerable uncertainty. That is, integration is done
533 over a time interval until the entire plume head volume has flown into the asthenospheric
534 channel. Hence the corresponding displacement vector in the center of the channel is

$$\mathbf{x}_{\text{plu}} = \int_{\Delta t} v_0 dt \mathbf{e}_r = \frac{r_p^3}{dh_c} \mathbf{e}_r$$

535 where \mathbf{e}_r is the unit vector radially away from the plume (red arrows in Supplementary Fig. 1).
536 Because of the parabolic flow profile, the vertical displacement gradient at the top of the channel
537 is

$$2 \frac{\mathbf{x}_{\text{plu}}}{0.5 h_c} = \frac{4}{h_c} \int_{\Delta t} v_0 dt \mathbf{e}_r = \frac{4r_p^3}{dh_c^2} \mathbf{e}_r.$$

538 Viscosity is defined such that the force per area is equal to viscosity times the radial gradient of
539 horizontal velocity. Hence the time integral of torque on the plate is

$$\mathbf{T}_{\text{plu}} = \frac{4\eta_0}{h_c} \int_A \mathbf{r} \times \mathbf{x}_{\text{plu}} dA = \frac{4\eta_0 r_p^3}{h_c^2} \int_A \frac{\mathbf{r} \times \mathbf{e}_r}{d} dA$$

540 where η_0 is viscosity in the channel and \mathbf{r} is the position vector. \mathbf{T}_{plu} is balanced by the time-
 541 integrated torque \mathbf{T}_{pla} of the plate rotating an angle $\boldsymbol{\omega}$ over the underlying mantle. With plate
 542 displacement vectors $\mathbf{x}_{\text{pla}} = \boldsymbol{\omega} \times \mathbf{r}$ (black arrows in Fig. S1) we obtain

$$\mathbf{T}_{\text{pla}} = -\frac{\eta_0}{h_s} \int_A \mathbf{r} \times \mathbf{x}_{\text{pla}} dA = -\frac{\eta_0}{h_s} \int_A \mathbf{r} \times (\boldsymbol{\omega} \times \mathbf{r}) dA.$$

543 Here h_s is an effective thickness of the layer over which shearing occurs, which is calculated
 544 below for a stratified viscosity structure, i.e. laterally homogeneous coupling of plate and mantle
 545 and which we will set equal to h_c for simplicity. Specifically, with \mathbf{T}_x being the time-integrated
 546 torque acting on a plate rotating an angle ω_0 around the x-axis

$$\mathbf{T}_x = -\frac{\omega_0 \eta_0}{h_s} \int_A \mathbf{r} \times (\mathbf{e}_x \times \mathbf{r}) dA$$

547 and \mathbf{T}_y and \mathbf{T}_z defined in analogy, the torque balance equation can be written

$$\mathbf{T}_{\text{plu}} = \frac{\omega_x}{\omega_0} \cdot \mathbf{T}_x + \frac{\omega_y}{\omega_0} \cdot \mathbf{T}_y + \frac{\omega_z}{\omega_0} \cdot \mathbf{T}_z.$$

548 ω_0 cancels out when \mathbf{T}_x , \mathbf{T}_y and \mathbf{T}_z are inserted. Integrals used to compute these torques only
 549 depend on plate geometry, η_0 cancels out in the torque balance, and we can solve for the rotation
 550 angle vector $\boldsymbol{\omega}$ simply by a 3 x 3 matrix inversion. In the more general case, where we do not set
 551 h_s and h_c equal, $\boldsymbol{\omega}$ is scaled by a factor h_s/h_c .

552 If a plate moves over a mantle where viscosity varies with depth, then the force per area
 553 F/A should be the same at all depths, and the radial gradient of horizontal velocity $dv/dz = F/A/\eta(z)$.
 554 If we assume that the deep mantle is at rest (i.e. it moves slowly compared to plate
 555 motions), we further find that plate motion is

$$v_0 = \int_{z_0}^{z(\eta_{\text{max}})} \frac{dv}{dz} dz = \frac{F}{A} \int_{z_0}^{z(\eta_{\text{max}})} \frac{1}{\eta(z)} dz =: \frac{F}{A} \cdot \frac{h_s}{\eta_0}. \quad (1)$$

556 The integration is done from the base of the lithosphere z_0 to the depth where the approximation
 557 of the “mantle at rest” is probably the most closely matched, i.e. we choose the viscosity
 558 maximum. The last equality is according to the definition of the effective layer thickness,

559 whereby η_0 is the viscosity just below the lithosphere. Solving this equation for h_s for the
560 viscosity structure in Supplementary Fig. 2 and a 100 km thick lithosphere gives $h_s=203.37$ km.

561 The plume location at 27.1°E, 40.4° S, is obtained by rotating the center of the
562 corresponding LIP at 46° E, 26° S and an age 87 Ma (adopted from Doubrovine et al.⁷³) in the
563 slab-fitted mantle reference frame⁴⁵, in which also the plate geometries at 105 Ma are
564 reconstructed.

565 Results for this case (Fig. 2A) show that a plume pushing one part of a plate may induce
566 a rotation of that plate, such that other parts of that plate may move in the opposite direction. A
567 simple analog is a sheet of paper pushed, near its bottom left corner, to the right: Then, near the
568 top left corner, the sheet will move to the left. With two sheets (plates) on either side, local
569 divergence near the bottom (near the plume) may turn into convergence near the top (at the part
570 of the plate boundary furthest away from the plume). The length of that part of the plate
571 boundary, where convergence is induced may increase, if one plate is nearly “pinned” at a hinge
572 point slightly NE of the plume, perhaps due to much stronger coupling between plate and mantle.
573 At the times considered here ~105 My ago, the Indian continent, where coupling was presumably
574 stronger, was in the southern part of the Indian plate, whereas in its north, there was a large
575 oceanic part, with presumably weaker coupling. Hence the geometry was indeed such that
576 convergence could be induced along a longer part of the plate boundary.

577 In the second case, we therefore consider lateral variations in the coupling between plate
578 and mantle, corresponding to variations in lithosphere thickness and/or asthenosphere viscosity,
579 by multiplying the drag force (from the first case) at each location with a resistance factor. This
580 factor is a function of lithosphere thickness reconstructed at 105 Ma. On continents, thickness
581 derived from tomography⁷⁴ with slabs removed⁷⁵ is simply backward-rotated. In the oceans, we
582 use thickness (km) = $10 \cdot (\text{age (Ma)} - 105)^{0.5}$ with ages from present-day Earthbyte age grid
583 version 3.6, i.e. accounting for the younger age and reduced thickness at 105 Ma, besides
584 backward-rotating. To determine the appropriate rotation, the lithosphere (in present-day
585 location) is divided up into India, Africa, Arabia, Somalia and Madagascar (paleo-)plates and
586 respective 105 Ma finite rotations from van der Meer et al.⁴⁵ are applied. For the parts of the
587 reconstructed plates where thickness could not be reconstructed in this way – often, because this
588 part of the plate has been subducted – we first extrapolate thickness up to a distance ~2.3°, and

589 set the thickness to a default value of 80 km for the remaining part. Reconstructed thickness is
590 shown in Supplementary Fig. 4. For the resistance factor as a function of lithosphere thickness
591 we use two models: Firstly, we use a continuous curve (Supplementary Fig. 3) according to eq.
592 (1)

$$\frac{F}{A} = \frac{v_0}{\int_{z_0}^{z(\eta_{\max})} \frac{1}{\eta(z)} dz} \quad (2)$$

593 with the mantle viscosity model in Supplementary Fig. 2 combined with variable lithosphere
594 thickness z_0 . However, this causes only a minor change in the plate rotations (Supplementary
595 Fig. 4 compared to Fig. 2B). Hence, we also use a stronger variation, further explained in the
596 caption of Fig 2 and with results shown in Fig. 2C and D.

597

598 **Data availability**

599 GPlates files with reconstructions used to draft Figure 1 are provided at
600 https://figshare.com/articles/dataset/van_Hinsbergen_NatureGeo_2021_GPlates_zip/13516727.

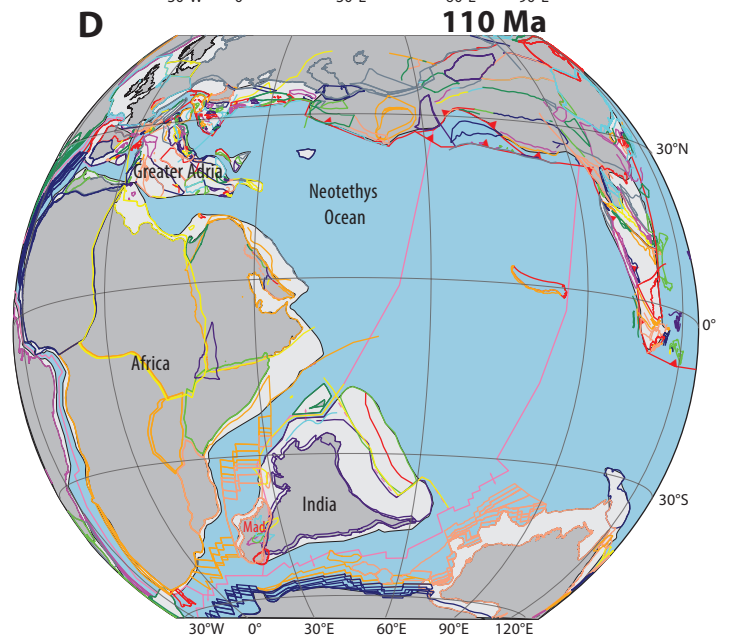
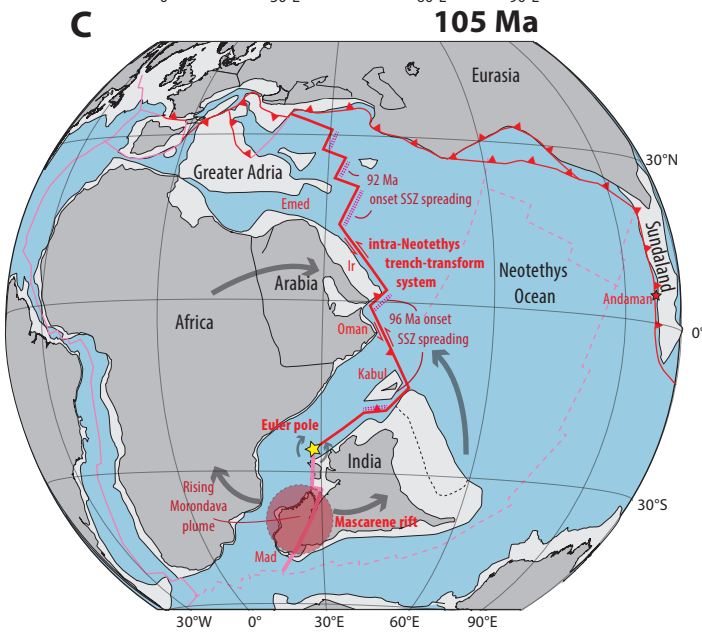
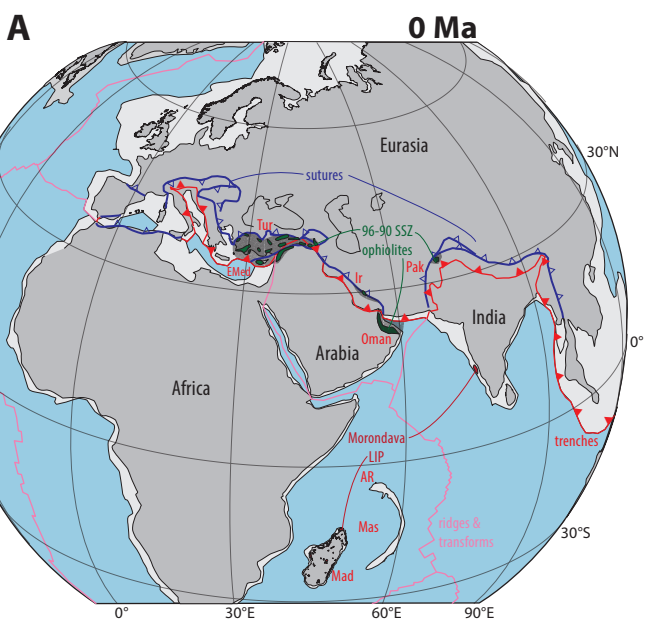
601

602 **Code availability**

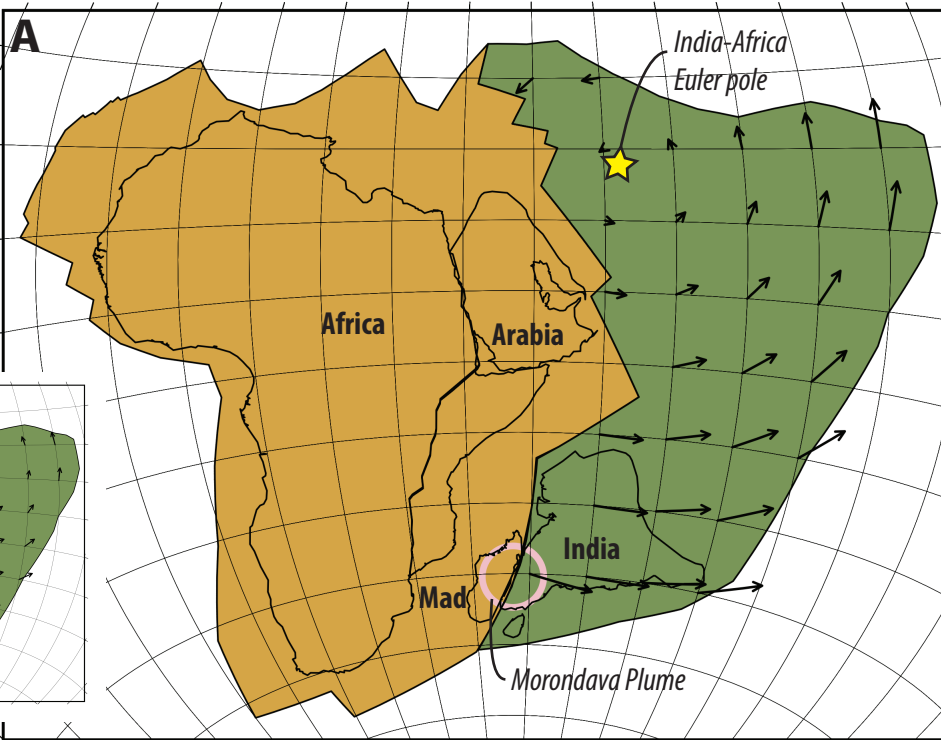
603 All codes used in the geodynamic modeling in this study are available at
604 https://figshare.com/articles/software/van_Hinsbergen_etal_NatureGeo_2021_geodynamics_package/13635089.

606

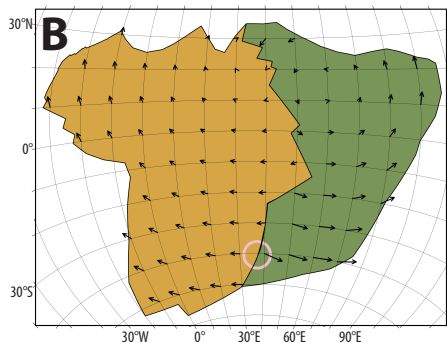
607



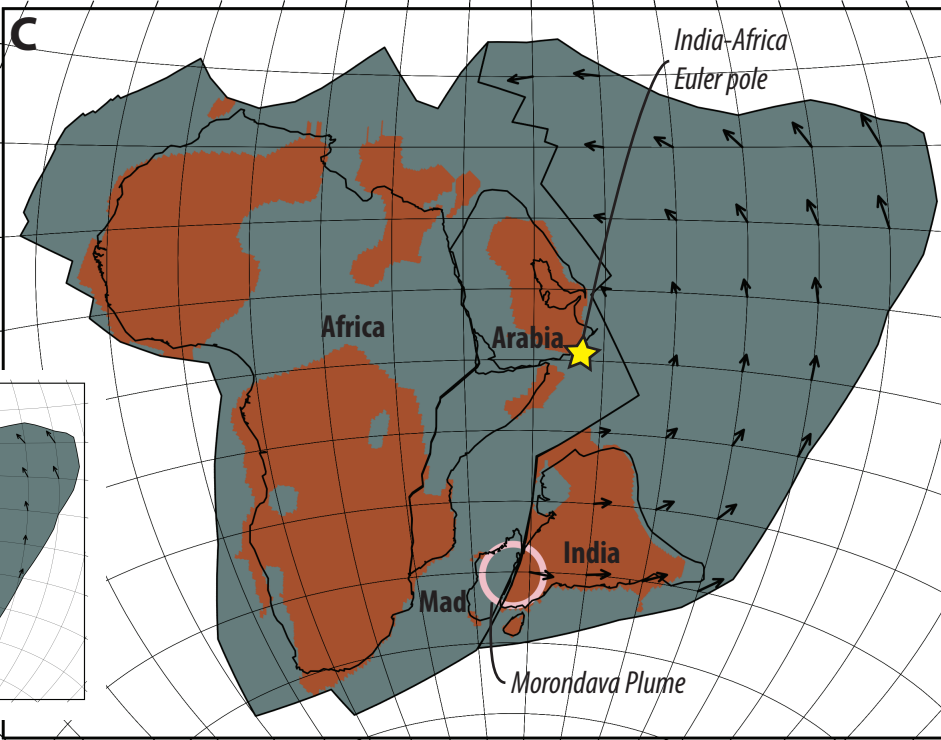
Africa-fixed frame



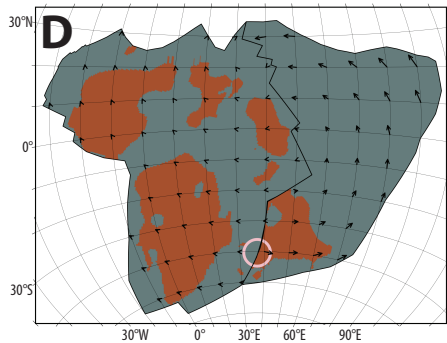
Mantle frame



Africa-fixed frame



Mantle frame



Supplementary Information

to

A record of plume-induced plate rotation triggering subduction initiation

Authors: Douwe J.J. van Hinsbergen^{1*}, Bernhard Steinberger^{2,3}, Carl Guilmette⁴, Marco Maffione^{1,5}, Derya Gürer^{1,6}, Kalijn Peters¹, Alexis Plunder^{1,7}, Peter J. McPhee¹, Carmen Gaina³, Eldert L. Advokaat^{1,5}, Reinoud L.M. Vissers¹, and Wim Spakman¹

Affiliations:

¹Department of Earth Sciences, Utrecht University, Princetonlaan 8A, 3584 CB Utrecht, Netherlands

²GFZ German Research Centre for Geosciences, Potsdam, Germany

³Centre of Earth Evolution and Dynamics (CEED), University of Oslo, Norway

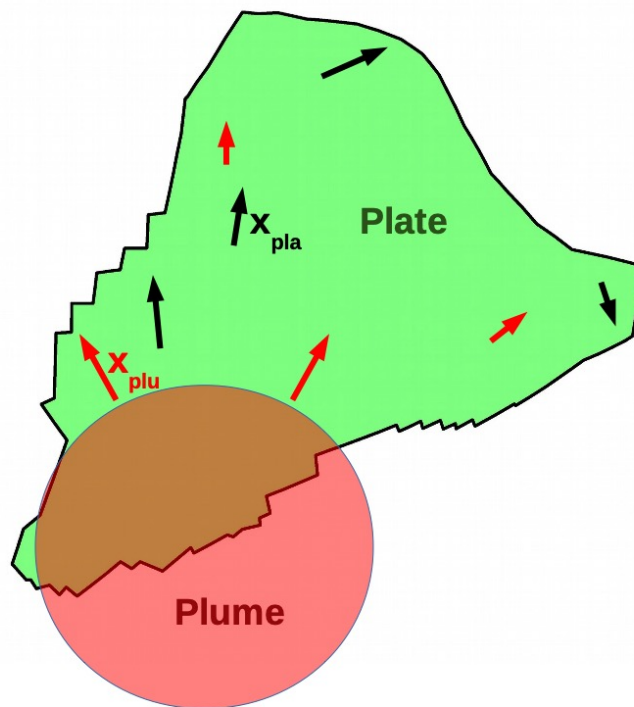
⁴Département de Géologie et de Génie Géologique, Université Laval, Québec, QC G1K 7P4, Canada

⁵School of Geography, Earth and Environmental Sciences, University of Birmingham, B15 2TT, UK

⁶School of Earth and Environmental Sciences, University of Queensland, St Lucia, Queensland 4072, Australia

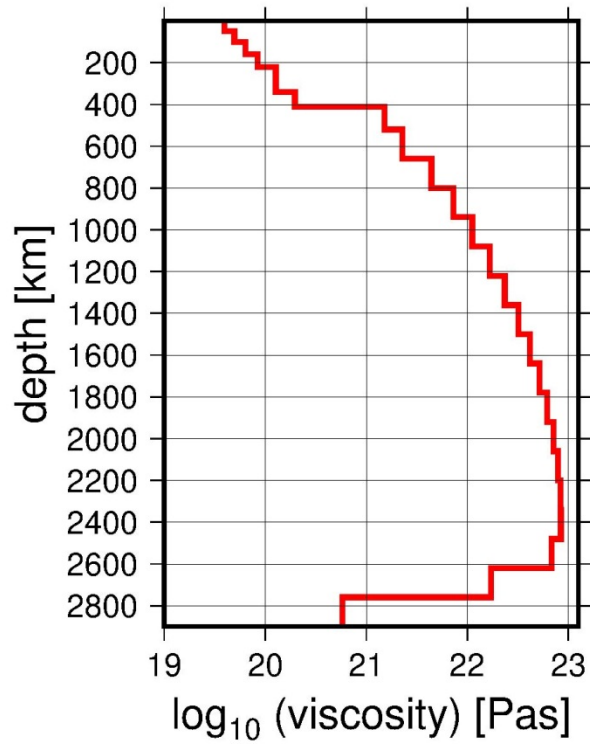
⁷BRGM, F-45060, Orléans, France

*Correspondence to: Douwe J.J. van Hinsbergen (d.j.j.vanhinsbergen@uu.nl)

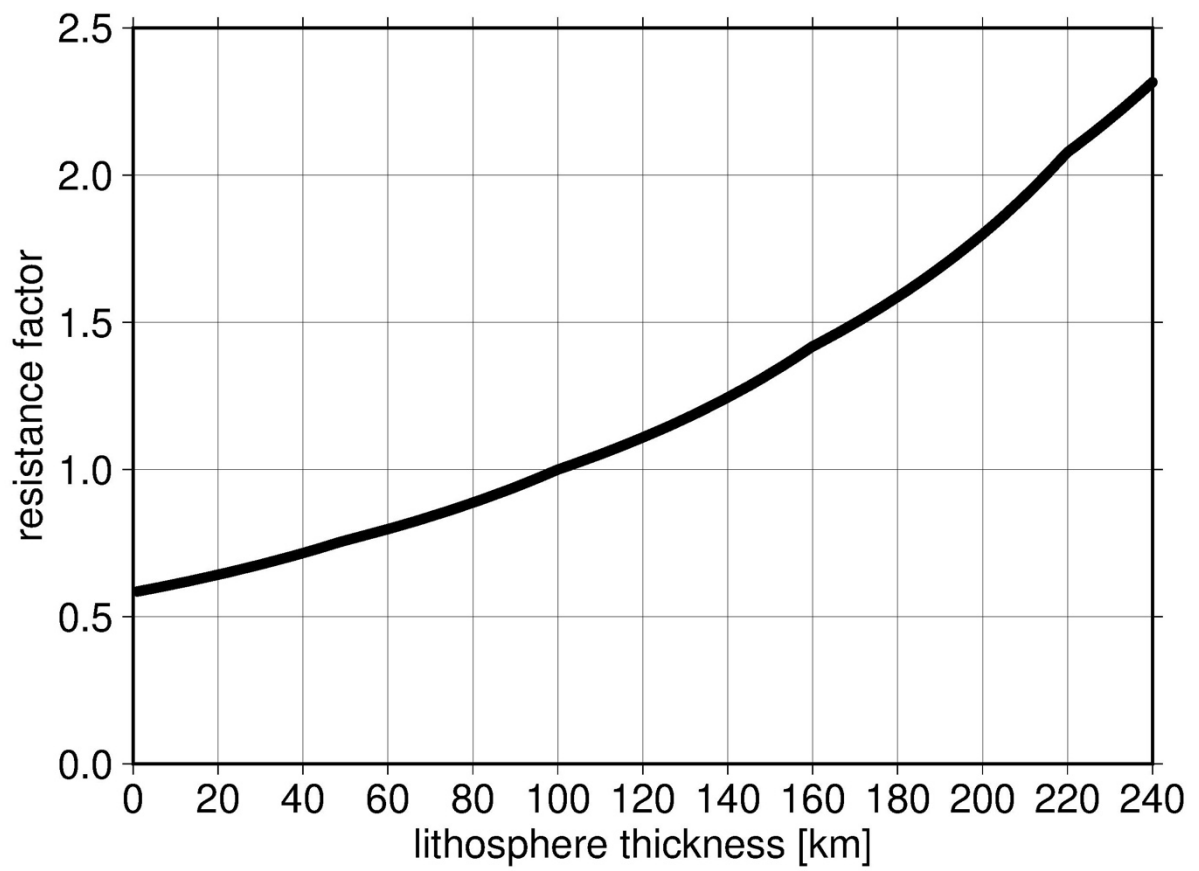


Supplementary Fig. 1: Sketch illustrating the geometry of a plume head hitting the boundary of a plate. Plume head in pink, not drawn to scale, plate in green. x_{plu} (red arrows) are the (maximum) displacement vectors in the asthenosphere caused by emplacement of the plume. Motion vectors of the plate x_{pla} (black arrows) correspond to the plate rotation ω that is caused. Reversal of direction from left to right indicates the rotational component of motion induced by the plume push. Note that, since plume push is modelled as Poiseuille

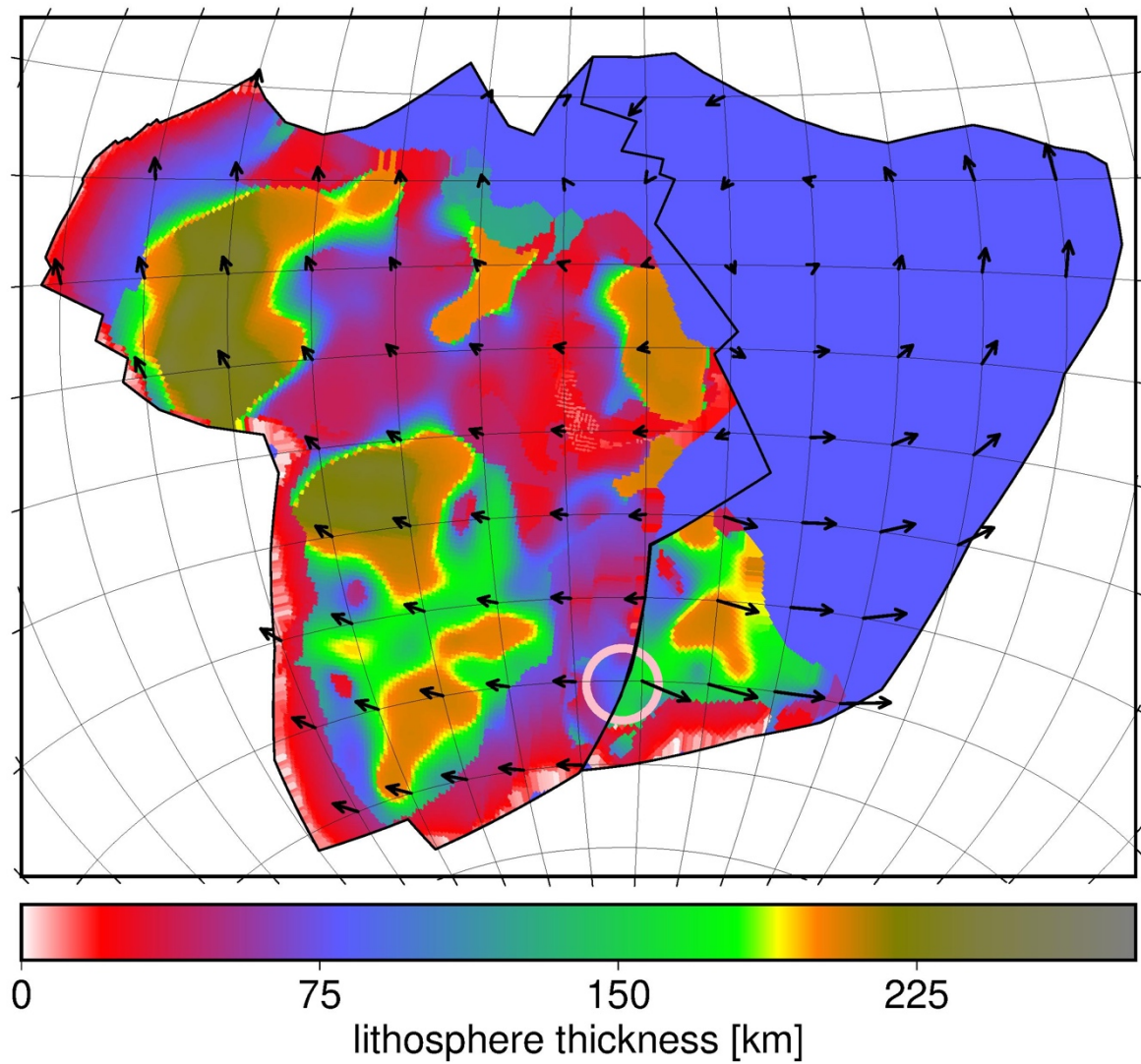
flow, the red arrows correspond to flow in the mid-asthenosphere, whereas plate motions induce Couette-type flow, therefore are shown at lithosphere depth.



Supplementary Fig. 2: Viscosity structure used. Structure is similar to Steinberger⁶⁶ but without lithosphere. This is being combined with a lithosphere of constant or variable thickness.



Supplementary Fig. 3: Resistance factor. Resistance factor to account for laterally variable coupling between lithosphere and mantle as a function of lithosphere thickness, for sub-lithospheric viscosity as in Supplementary Fig. 2, according to eq. (2).



Supplementary Fig. 4: Computed total amount of displacement induced by the Morondava plume considering lithosphere thickness variations. It is assumed that, compared to a case with no lateral variations, the drag force due to the plate moving over the mantle is multiplied at each location with a resistance factor according to Supplementary Fig. 3. Plates, plume (pink circle) and lithosphere thickness are reconstructed in the slab-fitted mantle reference frame⁴⁶.